The Astrophysical Journal, 781:15 (13pp), 2014 January 20 doi:10.1088/0004-637X/781/1/15

VACUUM ULTRAVIOLET EMISSION SPECTRUM MEASUREMENT OF A MICROWAVE-DISCHARGE HYDROGEN-FLOW LAMP IN SEVERAL CONFIGURATIONS: APPLICATION TO PHOTODESORPTION OF CO ICE

Y.-J. Chen[1,2], K.-J. Chuang[2], G. M. Muñoz Caro[3], M. Nuevo[4,5], C.-C. Chu[2], T.-S. Yih[2], W.-H. Ip[6], and C.-Y. R. Wu[1]
[1] Space Sciences Center and Department of Physics and Astronomy, University of Southern California, Los Angeles, CA 90089-1341, USA; yujung@usc.edu
[2] Department of Physics, National Central University, Jhongli City, Taoyuan County 32054, Taiwan
[3] Centro de Astrobiología, INTA-CSIC, Torrejón de Ardoz, E-28850 Madrid, Spain
[4] NASA Ames Research Center, Moffett Field, CA 94035, USA
[5] SETI Institute, Mountain View, CA 94043, USA
[6] Graduate Institute of Astronomy, National Central University, Jhongli City, Taoyuan County 32049, Taiwan
Received 2013 September 6; accepted 2013 November 21; published 2013 December 30

ABSTRACT

We report measurements of the vacuum ultraviolet (VUV) emission spectra of a microwave-discharge hydrogen-flow lamp (MDHL), a common tool in astrochemistry laboratories working on ice VUV photoprocessing. The MDHL provides hydrogen Ly-α (121.6 nm) and H_2 molecular emission in the 110–180 nm range. We show that the spectral characteristics of the VUV light emitted in this range, in particular the relative proportion of Ly-α to molecular emission bands, strongly depend on the pressure of H_2 inside the lamp, the lamp geometry (F type versus T type), the gas used (pure H_2 versus H_2 seeded in He), and the optical properties of the window used (MgF_2 versus CaF_2). These different configurations are used to study the VUV irradiation of CO ice at 14 K. In contrast to the majority of studies dedicated to the VUV irradiation of astrophysical ice analogs, which have not taken into consideration the emission spectrum of the MDHL, our results show that the processes induced by photons in CO ice from a broad energy range are different and more complex than the sum of individual processes induced by monochromatic sources spanning the same energy range, as a result of the existence of multistate electronic transitions and discrepancy in absorption cross sections between parent molecules and products in the Ly-α and H_2 molecular emission ranges.

Key words: astrochemistry – methods: laboratory: molecular – molecular processes – ultraviolet: ISM

Online-only material: color figures

1. INTRODUCTION

In recent decades, a considerable number of experimental studies have been carried out on the photochemistry of cosmic-ice analogs. These studies have provided invaluable insight and data to support astronomical observations and consequently improved our understanding of chemical evolution in astrophysical environments. A number of different photon sources have been used in these laboratory experiments (Westley et al. 1995; Watanabe et al. 2000, 2007; Wu et al. 2002; Cottin et al. 2003; Lee et al. 2009). The most widely used source is the microwave-discharge hydrogen-flow lamp (MDHL), because it provides intense Ly-α (or H I line) emission at 121.6 nm and molecular H_2 emission bands in the 140–170 nm range, with a flux of order 10^{15} photons s^{-1} (Warnek 1962). Such a continuous emission spectrum is believed to be a good analog of the diffuse interstellar UV field (Jenniskens et al. 1993; Muñoz Caro & Schutte 2003), which is often chosen in studies aiming at simulating photoprocesses of molecular species in space (Gerakines et al. 2000; Cottin et al. 2003; Loeffler et al. 2005; Öberg et al. 2007; Muñoz Caro et al. 2010).

In cold, dense interstellar regions, where temperatures can be as low as 10 K, most molecules are expected to condense onto grains and consequently be depleted in the gas phase. CO is mostly frozen out in these environments, although it is sometimes observed in the gas phase in cold molecular clouds such as IC 5146 and LDN 977 (Alves et al. 1999; Bergin et al. 2001). Mechanisms that have been proposed to explain why CO is not fully condensed in dense clouds include UV-induced photodesorption (Tielens & Hagen 1982; Prasad & Tarafdar 1983; d'Hendecourt et al. 1985; Cecchi-Pestellini & Aiello 1992), cosmic-ray whole-grain heating (Willacy & Millar 1998), cosmic-ray spot heating (Léger et al. 1985), and chemical desorption of weakly bound molecules (Duley & Williams 1993). Among these, a photodesorption mechanism involving chemical energy release induced by UV photolysis in the ice mantles of dust grains was proposed by Greenberg and coworkers (Greenberg & Yencha 1973; d'Hendecourt et al. 1982; Schutte & Greenberg 1991). Shen et al. (2004) reported a model of CO desorption from cosmic-ray-induced UV photons and showed that such a yield is almost an order of magnitude larger than that directly induced by cosmic-ray particles, while other desorption mechanisms could not explain astronomical observations. A more recent study in which pure CO ice was irradiated with an MDHL at 15–18 K showed a photodesorption yield of 2.7×10^{-3} molecules $photon^{-1}$ (Öberg et al. 2007). In contrast, Muñoz Caro et al. (2010) reported photodesorption yields for CO ice irradiated with an MDHL at 8 and 15 K of 5.4×10^{-2} and 3.5×10^{-2} molecules $photon^{-1}$, respectively, which is one order of magnitude larger than the values reported by Öberg et al. (2007).

Lu et al. (2005) measured the absorption cross section of CO ice in the 107–163 nm range and showed that at 121.6 nm (Ly-α), it is significantly lower than that in the 140–160 nm range. Fayolle et al. (2011) used tunable synchrotron radiation to irradiate CO ice and quadrupole mass spectrometry to detect the resulting desorbed CO molecules. They measured relatively low photodesorption yields at 121.6 nm, compared with those

measured at wavelengths coinciding with transitions to the first excited electronic state of CO. These two results indicate that the proportion of Ly-α photons in the 110–180 nm range is critical for the photodesorption yields of CO, so that differences in the contribution of the Ly-α emission in various UV sources could explain the discrepancies observed in the experimental results reported by Öberg et al. (2007) and Muñoz Caro et al. (2010) for the photodesorption yield of CO ice.

A large number of photochemical studies of interstellar ice analogs have attempted to measure destruction and production yields (or rates) of species applicable to astrophysical observations or models using an MDHL (Westley et al. 1995; Gerakines et al. 1996; Moore & Hudson 1998; Cottin et al. 2003; Leto & Baratta 2003; Loeffler et al. 2005; Palumbo et al. 2006; Bennett & Kaiser 2007; Watanabe et al. 2007; Öberg et al. 2007; Muñoz Caro et al. 2010). Only a few others have used a monochromatic light source (such as synchrotron radiation; Wu et al. 2002, 2003, 2012). However, the majority of these studies do not provide any UV output spectrum of the light source used, or any detailed information about their experimental conditions, and assume that the UV photon source is dominated by Ly-α emission, while the photon flux calibration and measurement of the sources is critical to determining photodepletion and photodesorption yields. In the present study, *photodepletion* refers to the decrease of the CO ice column density during photon irradiation, as the result of photolysis and photodesorption.

The method most widely used for photon flux calibration is actinometry, which is based on the photolytic conversion of O_2 into O_3 (Gerakines et al. 2000; Cottin et al. 2003). However, the absorption spectrum of O_2 ice in the vacuum ultraviolet (VUV) region shows that its absorption cross section is not constant over the full studied range, so that the photon flux calibration will be significantly affected if the VUV light source employed is not monochromatic (Mason et al. 2006; Cruz-Diaz et al. 2013). Furthermore, the use of a commercial silicate photodiode to measure the photon flux of the MDHL in the laboratory (Cottin et al. 2003; Öberg et al. 2007; Watanabe et al. 2007) can lead to an overestimated photon flux measurement if the photodiode is placed directly in front of the MDHL, as the photoelectric efficiency of such silicate photodiodes is non-negligible in the visible part of the spectrum, although often neglected. In this study, we use a nickel mesh calibrated for its photoelectric efficiency to monitor the photon flux of our MDHL during irradiation. The photon flux calibration protocol is described in detail in Sections 2 and 3.

The main purpose of our study is to demonstrate the effects of the experimental operating parameters and configurations of the MDHL on the photodesorption yield of pure CO ice at 14 K, and on the resulting photoproduction yield of CO_2. For this purpose, we operated the MDHL in four different configurations, each one affecting the average photon energy of the lamp, ranging from 8.6 to 10.0 eV, and the energy distribution of these photons. Our results are discussed in the context of understanding the difference between using a combination of several emission lines and using a monochromatic source. This way, we experimentally show through the irradiation of CO ice that processes induced by photons from a broad energy range are different and more complex than the sum of individual photoinduced processes, because of the existence of multistate electronic transitions and the discrepancy in absorption cross section between parent molecules and products in the Ly-α and H_2 molecular emission ranges. Therefore, the spectrum of the lamp must be characterized accurately for astrochemical laboratory studies of ice VUV photoprocessing.

2. EXPERIMENT

2.1. Measurement of the Photoelectric Efficiency of the Nickel Mesh

Metallic meshes are a reliable means for monitoring photon flux in situ and in real time during VUV irradiation. For this study, we chose an 88% transmittance nickel mesh (Precision Eforming), and an SXUV 100 photodiode (International Radiation Detectors), which was calibrated by NIST to measure the photoelectric efficiency of the nickel mesh in the 114–250 nm range. Using the high-flux beam line of the National Synchrotron Radiation Research Center in Hsinchu, Taiwan, which provides a VUV continuum in the 62–250 nm range, we measured the photoelectric efficiency of the nickel mesh between 114 and 250 nm with a great accuracy. This measurement was obtained by shining the synchrotron light through an MgF_2 window (VUV grade, Alkor Technologies), and then through the nickel mesh, before irradiating the surface of the photodiode. Since the photodiode was placed behind the nickel mesh, the induced photon current of the mesh was directly proportional to the photon flux measured on the surface of the photodiode.

2.2. Measurement of the VUV Spectra of the MDHL

VUV spectra of the MDHL were recorded by using a 1 m focal length monochromator (Seya-Namioka, McPherson, Inc.) set to a resolution of 0.33 nm and equipped with an osmium-coated 600 lines mm^{-1} grating. The VUV detector consisted of a quartz window coated with sodium salicylate and attached to a photomultiplier tube (R928, visible range, Hamamatsu Photonics). The coating was produced by dissolving sodium salicylate powder in methyl alcohol as a saturated solution and then spraying it onto the quartz window. A heating gun was used to blow hot air onto the window to facilitate the evaporation of the alcohol. This process can produce sodium salicylate films with fine crystalline layers (Samson 1967). A solar-blind photomultiplier tube could have been used instead, but no information about the transmittance was available for the photomultiplier, and its quantum efficiency is known to vary as a function of the wavelength. In contrast, the conversion efficiency of sodium salicylate (maximum fluorescence at 430 nm) is relatively constant throughout the 30–200 nm range, and its fluorescence decay time is about 10 ns (Samson 1967). Thus, the quartz window coated with sodium salicylate attached to a photomultiplier tube appears to be the best choice to measure VUV spectra and compare their relative intensities, although the absolute quantum efficiency of sodium salicylate varies with its thickness (Nygaard 1964) and decreases with time (Knapp & Smith 1964). In the present study, however, sodium salicylate was only used to measure the relative intensities of a few VUV spectra, each measured within 10 minutes, so that these limitations did not affect our measurements.

Finally, we used two different types of window, namely, MgF_2 and CaF_2, and two types of UV lamp, T type and F type, which differ in their geometry (Figure 1). Both lamps were made of quartz and designed in our laboratory. The F-type lamp is similar to any commercial UV lamp usually sold by Opthos Instruments and used by most research teams in the world. For both T-type and F-type lamps, the diameter of the quartz tube was 1/2 inch (12.7 mm) and the distance between the cavity and the window was about 110 mm.

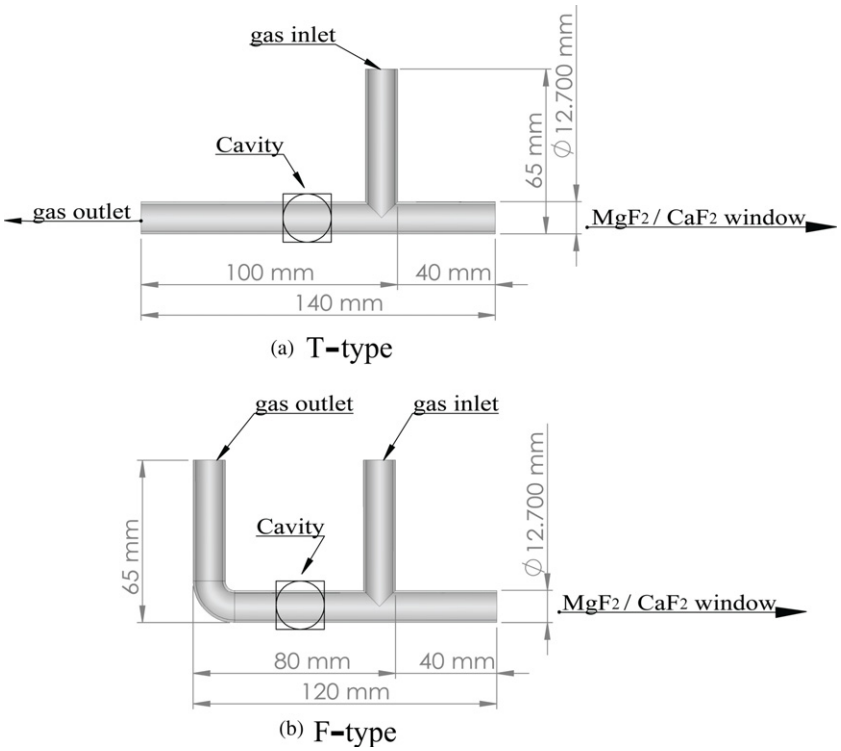

Figure 1. Schematic diagrams of the quartz-lamp geometries used in this study.

2.3. Experimental Setup

The basic experimental setup and protocol are described in detail in Chen et al. (2007), but since the publication of that paper, we significantly improved our vacuum condition as well as the signal-to-noise ratio for our spectroscopic measurements in the mid-infrared range. The so-called interstellar photoprocess system (IPS) consists of a main system, a gas-line system and a detection system, as illustrated in Figure 2 and described in detail in the following.

1. The main system consists of an ultra-high-vacuum (UHV) chamber equipped with a closed-cycle helium cryostat (CTI-M350). This chamber is pumped by a turbomolecular pump (KYKY FF-160/620ZE, capacity 600 liters s^{-1}), which is backed up by a dry pump (Alcatel Drytel 31) and a non-evaporation getter pump (SAES GP 50). The latter is very useful to absorb residual H_2, CO, and N_2 molecules in the chamber and helps to obtain a better signal-to-noise ratio for the mass spectra recorded by the quadrupole mass spectrometer (QMS) when monitoring the desorption of CO (see Section 3.3.3). The pressure in the UHV chamber, which can reach down to 1×10^{-10} torr, is monitored by a Granville–Phillips 370 Stabil-Ion gauge. A KBr window is attached to the sample holder and used as a substrate for ice deposition. The cold finger to which the sample holder is attached is made of oxygen-free copper and is mounted on the tip of the cryostat, where the temperature can go down to 14 K. The tip of the cold finger, where the sample holder is located, is protected by a radiation shield mounted on the first stage of the cryostat, and where the temperature is 77 K. All the parts of the cold finger are connected with indium (99.99% purity) to ensure perfect thermal conductivity over its length. Finally, two silicon diode sensors (LakeShore DT-670-SD) are used to simultaneously monitor the temperature at the sample location, which can be controlled with a 0.1 K accuracy from 14 to 400 K thanks to a LakeShore 331S temperature controller equipped with a tunable heater, and at the tip of the cryostat.
2. Our gas-line system is a stainless steel line containing four stainless steel bottles of the same volume, which are used to determine the relative proportions between the components of our gas mixtures through their partial pressures. Partial pressures are measured with an MKS 622A Baratron gauge in the 0–10 torr range with a 0.25% accuracy. The gas line is pumped by a turbomolecular pump (Oerlikon Leybold TurboVac 151, capacity 145 liters s^{-1}), which is backed up by an oil-sealed mechanical pump (Alcatel 2012A, capacity 450 liters $minute^{-1}$) equipped with an oil trap (molecular sieve type 13X). The background pressure in the gas line is routinely lower than 1×10^{-7} torr. When not used to mix gases, the system is continuously baked at 120°C in order to avoid any organic contamination.
3. Our detection system consists of a mid-infrared Fourier transform spectrometer (mid-FTIR) and a QMS. The mid-FTIR (ABB FTLA2000-104) is equipped with a mercury–cadmium–telluride detector. For this study, infrared spectra were acquired with a resolution of 2 cm^{-1} and averaged over 128 scans. In order to avoid atmospheric water vapor and carbon dioxide gas contamination on the IR spectra, the IR beam path was built under vacuum, so that there are almost no absorption features of CO_2 gas in the 2390–2300 cm^{-1} range and that the measurement limit of solid CO_2 reaches 0.1 monolayers (ML) in this study ($1\ ML = 10^{15}$ molecules cm^{-2}). The angle between the substrate and the IR beam is 45°. The QMS (Stanford Research Systems RGA300, equipped with an electron multiplier) is located 10 cm from the substrate and run with a resolution better than 0.5 atomic mass units (amu). Mass spectrometry can be used to monitor the sample purity during the deposition process and to measure the signal intensity of VUV-induced photodesorbed CO ice.

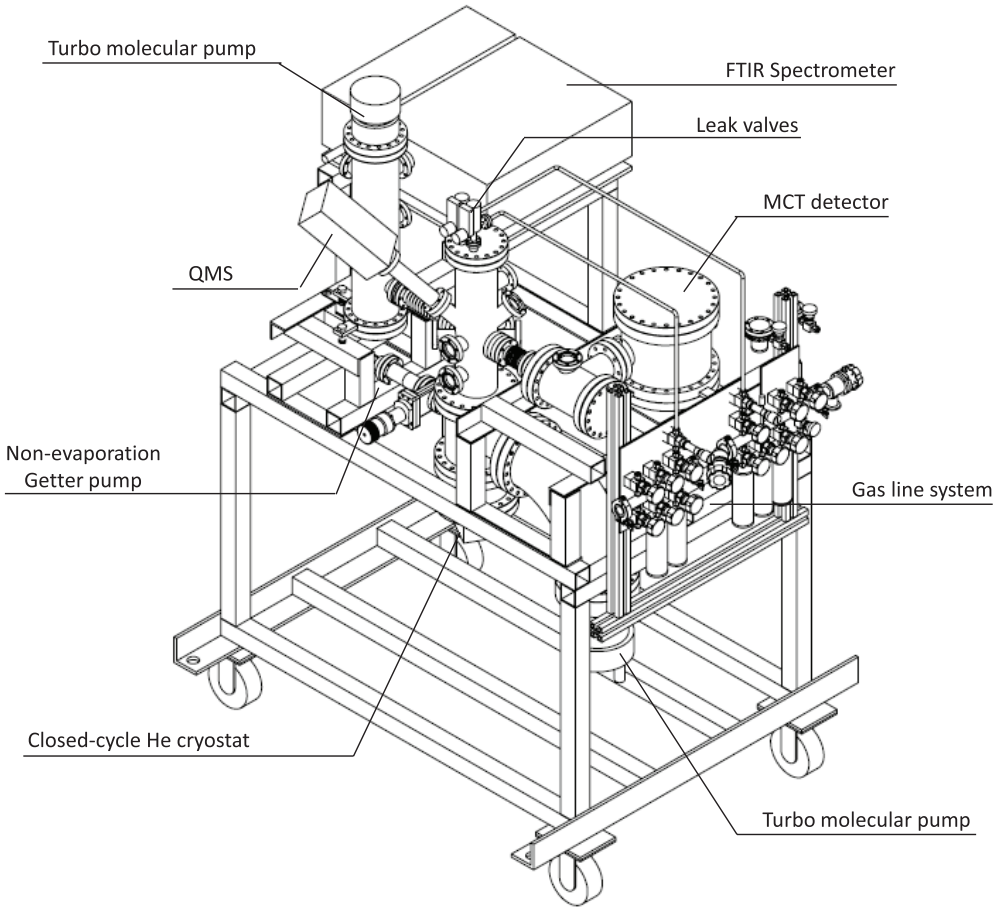

Figure 2. Schematic diagram of the IPS experimental setup.

The VUV photon source chosen for this study is an MDHL equipped with either an MgF_2 or a CaF_2 window and run with a gas flow of either pure hydrogen (H_2) or a mixture of H_2 and helium (He). Since the VUV beam of the MDHL is divergent, we placed an optically polished quartz tube between the MgF_2/CaF_2 window and the substrate in order to collimate the VUV beam. Such a configuration also helps to avoid VUV photons reaching the inner walls of the UHV chamber and the substrate holder and thus helps to control the amount of contaminating CO_2 originating from outside the sample substrate. The photon flux of the MDHL equipped with such a quartz tube was measured to be about five times higher than that of a lamp without the tube. A nickel mesh, used for in situ measurement of the photon flux, was placed at the end of the quartz tube, close to the KBr substrate. Finally, the size of the VUV beam was nearly 100 mm^2 on the KBr window at the substrate position.

2.4. Experimental Protocol

Before any experiment was performed, the IPS was baked at 100°C for 48 hr to reduce water contamination as much as possible. It was then cooled to room temperature, at which the background pressure in the chamber is routinely in the $\sim 1 \times 10^{-10}$ torr range. Before cooling the substrate to cryogenic temperatures, an IR spectrum and a mass spectrum of the UHV chamber were recorded, in order to compare them with any IR and mass spectra further recorded at 14 K and verify the presence of any potential contaminants in the chamber. Prior to the preparation of CO, the gas line was first cooled to room temperature. Once the substrate had been cooled to 14 K, the flow of CO gas was allowed into the UHV chamber through a 1/4 inch (6.35 mm) stainless steel bellows connecting the UHV chamber and the gas line and a 1 mm diameter capillary placed 20 mm away from the substrate inside the chamber. A CO ice deposition rate of $\sim$0.1 ML s^{-1} was controlled by a leak valve (VG Scienta LVM series). During deposition, the purity of the CO ice was monitored by QMS and the ice thickness derived from both IR spectroscopy and the interference intensity of a 532 nm solid-state laser.

After deposition of CO, we waited 10–15 minutes until the background mass spectrum reached a level comparable to that before deposition. An IR spectrum was recorded before irradiation of the CO ice, and the column density of the deposited ice calculated according to

$$N = \int_{\text{band}} \frac{\tau_\nu d\nu}{A}, \quad (1)$$

where N is the column density in molecules per square centimeter, τ_ν is the optical depth of the band, ν is the wavenumber in inverse centimeters, and A is the band strength in centimeters per molecule. The band strength value used for CO at $\sim$2138 cm^{-1} was $A = 1.1 \times 10^{-17}$ cm $molecule^{-1}$ (Jiang et al. 1975).

The photon flux of the MDHL was monitored in situ by the nickel mesh calibrated for its photoelectric efficiency during VUV irradiation (see Section 3.2). Since the photon flux of the lamp is continuously monitored through the duration of these experiments, the total photon dose is calculated after integration over the whole irradiation time and correction of the flux according to the variation of the photon current measured

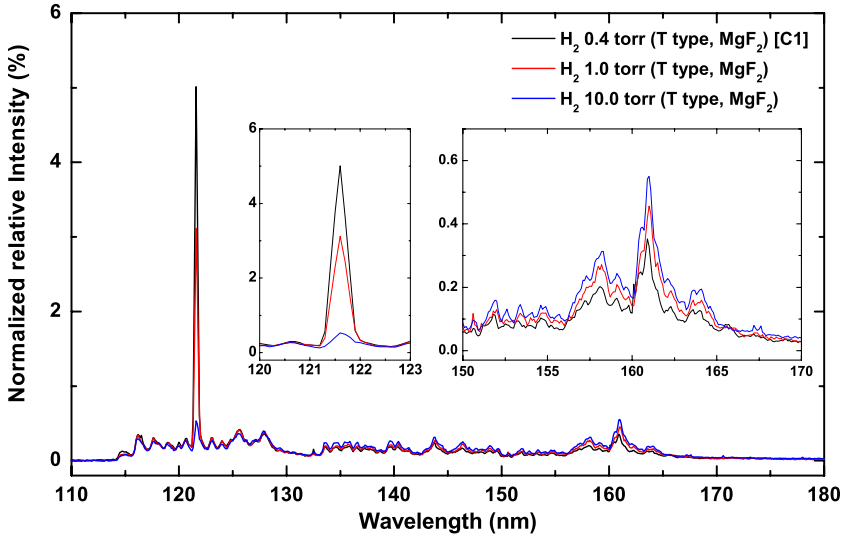

Figure 3. VUV spectra of the MDHL (T-type geometry, MgF_2 window) in the 110–180 nm range as a function of the pressure of molecular hydrogen flowing inside the lamp.

(A color version of this figure is available in the online journal.)

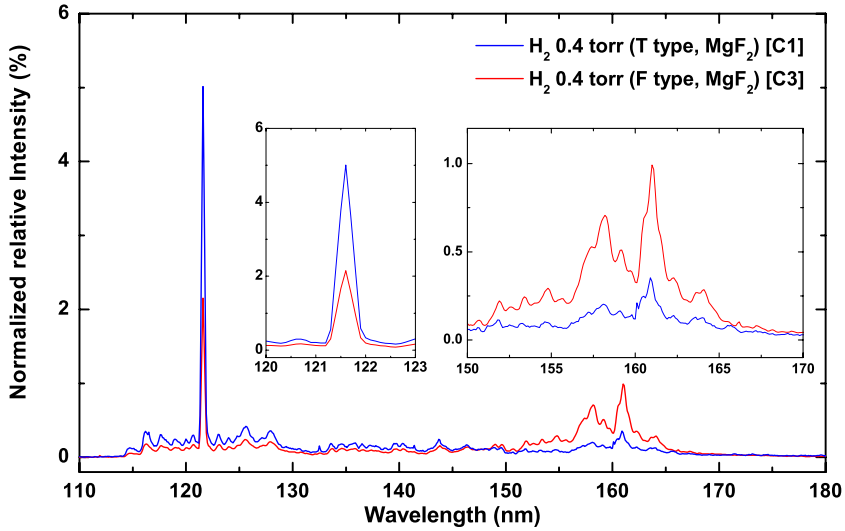

Figure 4. VUV spectra of the MDHL (0.4 torr H_2 pressure, MgF_2 window) in the 110–180 nm range as a function of lamp geometry: T type (blue line) or F type (red line).

(A color version of this figure is available in the online journal.)

by the nickel mesh. This method has been proven efficient for calculating photon doses with a high accuracy. VUV irradiation was stopped every time an IR spectrum was recorded, in order to calculate the photon dose as accurately as possible. Finally, after VUV irradiation the substrate was warmed to 300 K at a rate of 2 K $minute^{-1}$, during which time mass spectrometry was employed to record thermally desorbed species, including the parent molecule (CO) and its photoproducts (C_2O, C_3O, C_3O_2, etc.).

3. RESULTS AND DISCUSSION

3.1. VUV Spectra of the MDHL

In the following, we show how different parameters of the MDHL affect its VUV spectrum. Figure 3 shows the VUV spectra of the T-type MDHL in the 114–180 nm range for three different pressures of H_2 inside the lamp. These spectra highlight the important effect of this parameter on the relative intensities between the different emission features in the VUV range. The lower the hydrogen pressure, the higher the proportion of Ly-α photons, and vice versa. Indeed, the intensity of the Ly-α emission reaches its maximum when the H_2 pressure is 0.4 torr, while it almost disappears when the pressure is increased to 10.0 torr. The intensity of the molecular emission is also affected, decreasing with the H_2 pressure, although to a significantly lesser degree.

Figure 4 compares the VUV spectra in the same 114–180 nm range for the two different geometries of lamp studied, namely, F and T types (see Figure 1), for the same H_2 pressure of 0.4 torr in the lamp. These spectra clearly show that the T-type lamp increases the proportion of Ly-α emission, until it reaches 19.1% of the full integrated 114–180 nm range, while by comparison the proportion of Ly-α photons for the F-type lamp over the same range is less than half (8.4%). In addition, Figure 4 indicates that the use of the T-type lamp can significantly decrease the contribution of the molecular hydrogen emission

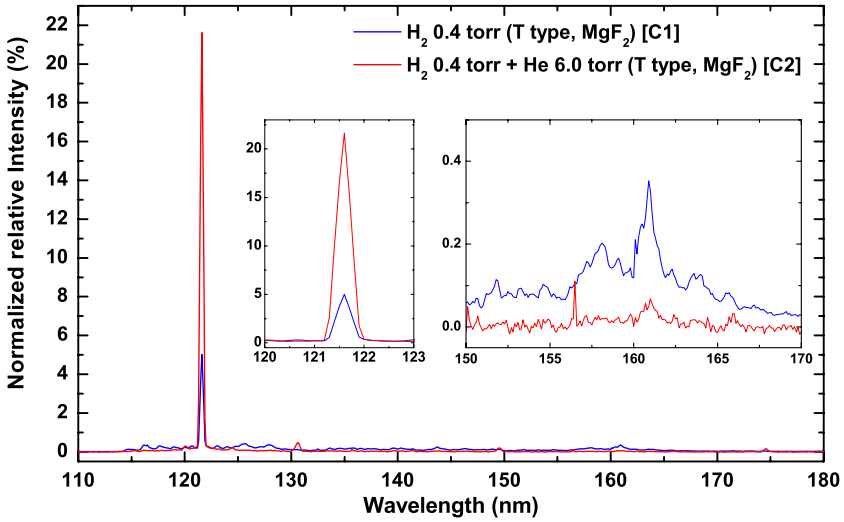

Figure 5. VUV spectra of the MDHL (T-type geometry, MgF_2 window) in the 110–180 nm range comparing the nature of the gas flowing in the lamp, namely, pure molecular hydrogen (0.4 torr, blue line) versus hydrogen seeded in helium (0.4 torr H_2 in 6.0 torr He, red line). The H_2/He mixture increases the proportion of the Ly-α emission and almost eliminates the contribution from the molecular hydrogen emission bands.

(A color version of this figure is available in the online journal.)

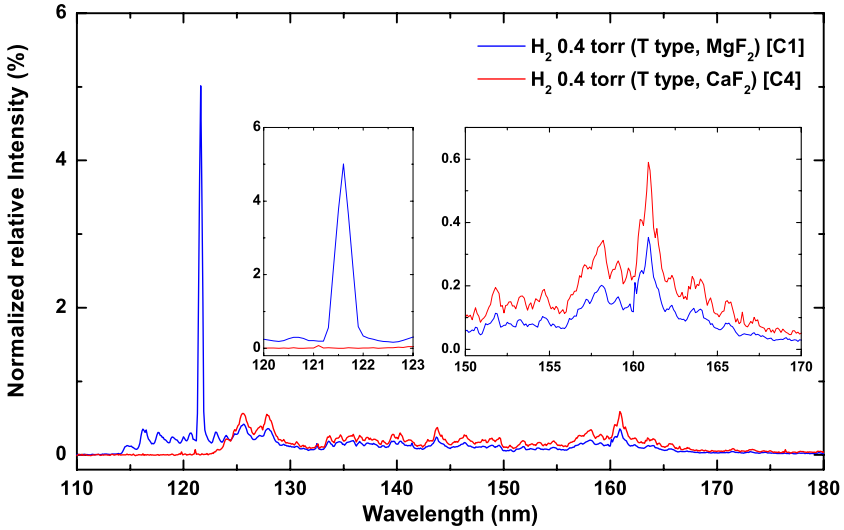

Figure 6. VUV spectra of the MDHL (0.4 torr H_2 pressure, T-type geometry) in the 114–180 nm range when equipped with either an MgF_2 (blue line) or a CaF_2 (red line) window.

(A color version of this figure is available in the online journal.)

bands, probably because the T-type geometry improves the pumping efficiency and thus allows more H_2 molecules to be evacuated from the area of the resonance cavity.

Figure 5 shows how the nature of the gas flowing in the (T-type) lamp affects its VUV spectrum. For this, we compared the spectrum obtained for a lamp running with a regular H_2 flow at a pressure of 0.4 torr with that of a lamp running with 0.4 torr of H_2 seeded in 6.0 torr of He. As shown in Figure 5, the use of the H_2/He gas mixture leads to an elimination of the molecular hydrogen bands, while the proportion of Ly-α emission in the 114–180 nm range increases to 76.4%. In addition, the VUV spectrum of the lamp running with 0.4 torr of hydrogen seeded in 6.0 torr of argon (not shown) leads to a proportion of Ly-α emission of 83.4% in the same wavelength range, but with a photon flux three times lower than for an H_2/He gas mixture. More generally, our VUV measurements show that the proportion of Ly-α emission in the 114–180 nm range can be made to exceed 90% by increasing the pressure of helium or argon, at the expense of the photon flux, which will decrease significantly.

Finally, Figure 6 compares the use of a CaF_2 window with that of the regular MgF_2 window between the lamp and the vacuum chamber and its effect on the VUV spectrum. Because of the 123 nm cutoff of CaF_2, the MDHL equipped with such a window provides a VUV light without Ly-α emission. This configuration can be useful for the study of photoprocesses involving only the effect of molecular hydrogen bands.

The optical quality of the MgF_2 window is another important parameter, although not studied in detail here, that affects the VUV spectra of the lamp. Indeed, the transmittance of MgF_2 in the 114–130 nm range varies strongly, and a poor-quality window affects the intensity of the Ly-α emission band relative to the others in the VUV region as well as the photon flux. In this study, we used a UV-grade MgF_2 window (Alkor), the transmittance of which at 121.6 nm was measured to be about 67%.

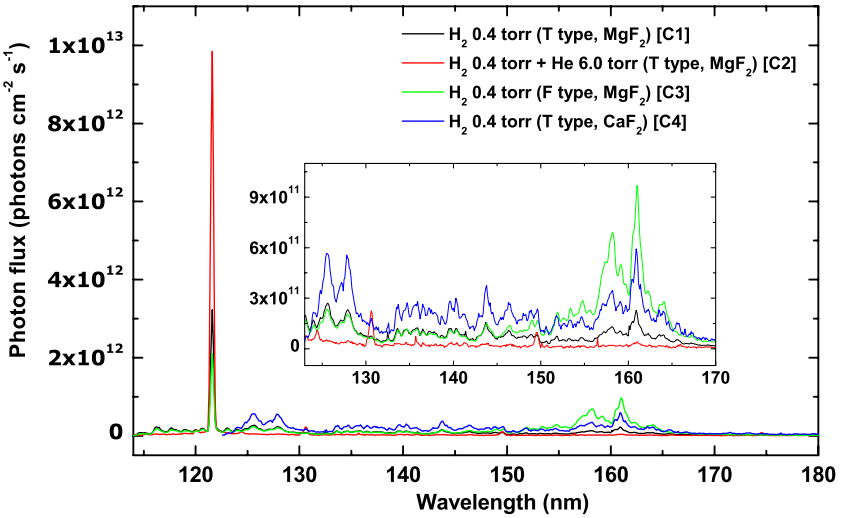

Figure 7. Photon flux distribution of the MDHL in the 114–180 nm range for the four configurations (see Table 1).
(A color version of this figure is available in the online journal.)

Table 1
MDHL Photon Data

Exp. No.	Operating Configuration of MDHL	Proportion of Ly-α (114–180 nm Range)	Average Energy (eV)	Photon Flux (photons cm^{-2} s^{-1})
C1	H_2 0.4 torr (T type, MgF_2)	19.1%	9.27	6.4×10^{13}
C2	H_2 0.4 torr + He 6.0 torr (T type, MgF_2)	76.4%	10.0	4.6×10^{13}
C3	H_2 0.4 torr (F type, MgF_2)	8.4%	8.60	9.8×10^{13}
C4	H_2 0.4 torr (T type, CaF_2)	0.0%	8.60	1.0×10^{14}

Note. The rightmost columns list the proportion of Ly-α emission relative to the total emission in the 114–118 nm range, average photon energy, and photon flux of the MDHL for the operating configurations C1–C4.

3.2. Photon Flux Calibration of the MDHL

The VUV spectra measured in the 114–180 nm range for the MDHL in different operating configurations provide information about the relative photon fluxes in each of them. Each spectrum measured was corrected by the reflectance of the grating, which depends on the photon wavelength, to obtain the relative intensity spectrum. This spectrum provides the photon energy distribution that irradiates our sample in the described experiments. As mentioned above, the transmittance of the MgF_2 window is a critical parameter, as its optical quality will affect the proportion of Ly-α and hydrogen molecular band emissions in the 114–180 nm range and may explain the discrepancies observed between the UV spectra measured for MDHLs by different groups (Weber & Greenberg 1985; Öberg et al. 2009; Muñoz Caro et al. 2010).

Using the measured relative photon energy distribution and the photoelectric efficiency of the nickel mesh, we can derive the relative photon current distribution, which is a function of the wavelength. By integrating the product of the relative photoelectric current and the photoelectric efficiency of the nickel mesh over the 114–180 nm range, we obtain a number equivalent to a photoelectric conversion factor, which depends on the MDHL operating configuration. Such a factor is necessary in order to derive the photon flux of the lamp from the photon current recorded by the nickel mesh during irradiation. In addition, the nickel mesh can be used for in situ and real-time monitoring of the photon flux. Another advantage of nickel is its work function, 5.15 eV; the contribution of the photons produced by the MDHL in the visible range are not included for estimating the VUV photon flux.

Table 1 shows the proportion of Ly-α photons in the 114–180 nm range, the average photon energy, and the photon flux measured for the MDHL under the four different operating conditions discussed in Section 3.1 and illustrated in Figures 3–6, referred to as C1–C4. Figure 7 compares the photon flux distributions of the MDHL as a function of wavelength for these four different operating conditions, obtained after taking the efficiency of the nickel mesh and its conversion factor into account.

Before the present study, photon fluxes for equivalent lamps were usually measured using AXUV100G photodiodes (Cottin et al. 2003; Öberg et al. 2007; Watanabe et al. 2007). However, these are known to have a high quantum efficiency in the visible range, which leads to an overestimate of the measured photon flux when the photodiode is placed in front of the lamp without using any well-characterized monochromatic light. In addition, research groups who used the actinometry method (based on the photoconversion of O_2 into O_3) to estimate the photon flux of the MDHL (Gerakines et al. 2000; Cottin et al. 2003; Leto & Baratta 2003) did not take into account the fact that the absorption cross section of O_2 ice in the VUV region is not constant. Therefore, the calibration of the photon flux will be affected when not using a monochromatic light source (Mason et al. 2006; Cruz-Diaz et al. 2013).

Figure 8 shows the photon current of the nickel mesh and indicates that the photon flux is not constant when the MDHL is turned on, although it reaches a fairly stable value after the MDHL has been running for 25–30 minutes. This affects the photodepletion and photoproduction rates measured during the first minutes of an experiment, and the precision on the value of the recorded photon flux becomes very important. It is therefore

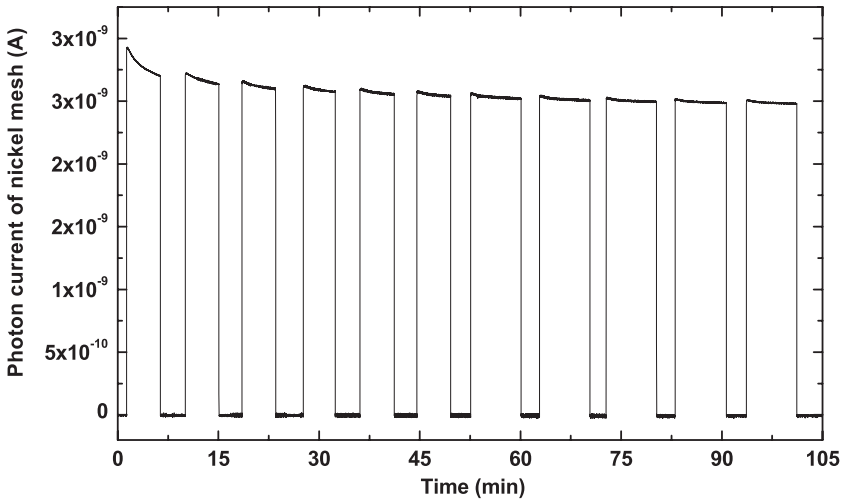

Figure 8. Photon current output of the MDHL recorded by an in-line nickel mesh during a typical VUV irradiation experiment. Between each actual irradiation of the ice, the MDHL output was blocked for IR spectroscopy and QMS measurements.

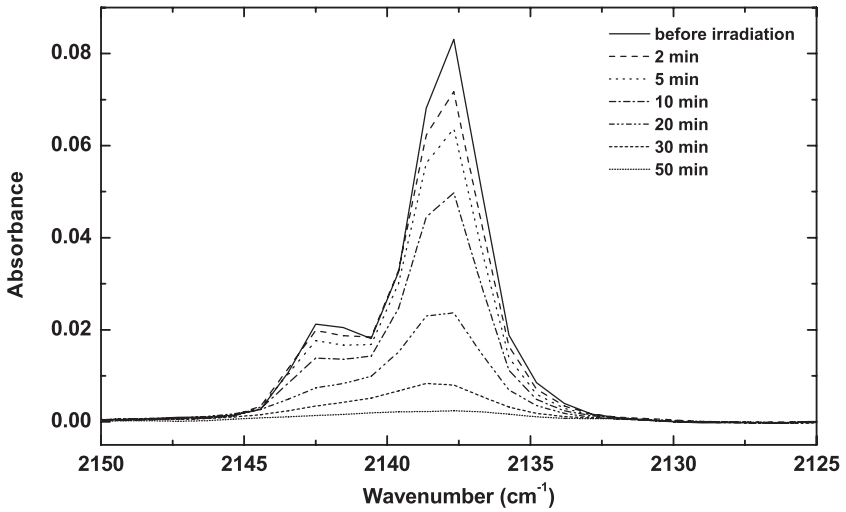

Figure 9. Absorbance variation of the 2138 cm^{-1} band of CO ice at 14 K as a function of VUV irradiation time (configuration C1).

recommended to leave the MDHL on for 30 minutes in order to allow the VUV flux to stabilize before starting any measurement.

3.3. VUV Irradiation of CO Ice at 14 K

In this study of VUV irradiation of CO ice at 14 K, we used the MDHL as a UV photon source in the four operating configurations C1–C4 illustrated in Table 1 and Figure 7. Thus, our CO ice samples were subjected to four different photon energy distributions, to assess their effect on the photodepletion and photodesorption yields of CO at 14 K. In the configuration in which we use a flow of H_2 seeded in He (C2), the proportion of Ly-α photons in the 114–180 nm range is the highest among our experiments (76.4%). In contrast, in the configuration in which the MDHL is equipped with a CaF_2 window instead of the regular MgF_2 window (C4), the 123.0 nm cutoff of CaF_2 suppresses the contribution of the Ly-α emission and photoprocesses are mostly driven by the molecular hydrogen band emission.

3.3.1. Photodepletion of CO Ice at 14 K

Figure 9 displays the IR absorbance of the CO ice band near 2138 cm^{-1} at 14 K (2 cm^{-1} resolution) before VUV irradiation and at different stages during irradiation (from 2 to 50 minutes). Because of the 45° angle of the substrate with respect to the IR beam, the absorption bands corresponding to *s* and *p* polarizations are observed. The corresponding column densities were calculated by integrating the absorption bands from 2120 to 2156 cm^{-1} at each stage of irradiation following Equation (1). The thickness of the CO ice before irradiation was monitored to be ∼22 ML in each experiment. Figure 10 shows the evolution of the column density of CO ice as a function of the photon dose for the four different configurations of the MDHL. For each configuration, the data points correspond to the average of three independent experiments. A linear correlation between the column density of CO and the photon dose in all experiments is observed for ice thicknesses larger than ∼4 ML (Figure 10, horizontal line). This result, which is consistent with previous studies (Muñoz Caro et al. 2010; Fayolle et al. 2011), implies that photons absorbed at deeper than 4 ML cannot transfer their energy to the surface and, therefore, cannot induce photodesorption. Öberg et al. (2007) and Muñoz Caro et al. (2010) both proposed photodesorption to be the main cause of the decrease of intensity of the CO ice absorption band around 2138 cm^{-1}, and both estimated that less than 5% of CO ice is destroyed and converted into CO_2 and other products.

Table 2
Comparison between IR Spectroscopy and QMS Data

Exp. No.	IR Spectroscopy			Mass Spectrometry	
	Photodepletion Yield[a] (molecules photon^{-1})	Photodesorption Yield[b] (molecules photon^{-1})	Normalized Ratio	Partial Photodesorption Yield[c] (A photon^{-1})	Normalized Ratio
C1	$(22.8 \pm 0.3) \times 10^{-2}$	$(21.2 \pm 0.3) \times 10^{-2}$	1.00	$(6.2 \pm 0.3) \times 10^{-22}$	1.00
C2	$(7.0 \pm 0.2) \times 10^{-2}$	$(6.4 \pm 0.2) \times 10^{-2}$	0.30	$(1.8 \pm 0.1) \times 10^{-22}$	0.29
C3	$(9.8 \pm 0.2) \times 10^{-2}$	$(8.9 \pm 0.2) \times 10^{-2}$	0.42	$(2.6 \pm 0.1) \times 10^{-22}$	0.42
C4	$(9.8 \pm 0.2) \times 10^{-2}$	$(8.3 \pm 0.2) \times 10^{-2}$	0.39	$(2.4 \pm 0.1) \times 10^{-22}$	0.39

Notes.
[a] Fitting results from Figure 10.
[b] Fitting results from Figure 12.
[c] Fitting results from Figure 14.

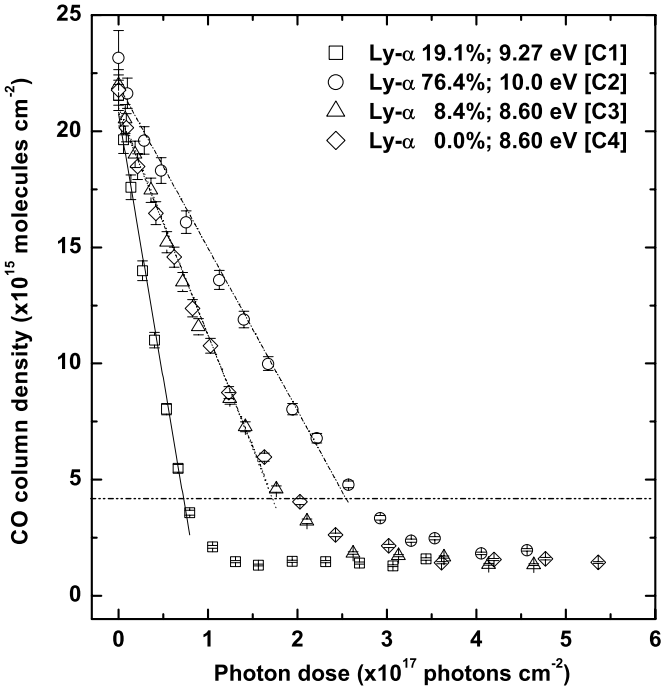

Figure 10. Decrease of the column density of CO ice as a function of photon dose for configurations C1–C4 (Table 1); 1 ML of CO ice is assumed to be equivalent to a column density of 10^{15} molecules cm^{-2}.

From the linear fits of the CO column densities shown in Figure 10, we found that the photodepletion yield induced mostly by Ly-α photons (configuration C2) is 7.0×10^{-2} molecules photon^{-1}, which is lower than that induced mostly by molecular hydrogen emission bands (configuration C4), determined to be 9.8×10^{-2} molecules photon^{-1} (Table 2). Lu et al. (2005) measured the VUV absorption spectrum of CO ice at 20 K and showed that its absorbance at 121.6 nm was dramatically low compared with the resonant features. Despite this, experimental results from Fayolle et al. (2011) indicate that the photodesorption yield of CO ice at 121.6 nm (10.2 eV) measured with a QMS is $(6.9 \pm 2.4) \times 10^{-3}$ molecules photon^{-1}, which is about four times smaller than the highest photodesorption yield, $(2.8 \pm 1.7) \times 10^{-2}$ molecules photon^{-1} at 151.2 nm (8.2 eV), in the resonant region. In contrast, when both Ly-α and molecular hydrogen emission photons irradiate CO ice simultaneously (configuration C1), the photodepletion yield is about three times higher than for configuration C2 (mostly Ly-α photons), and two times higher than for configuration C4 (mostly molecular hydrogen emission).

Based on the proportions of Ly-α photons and molecular hydrogen bands in the spectra measured for the MDHL in the four configurations, the photodepletion yield for configuration C1 would be expected to be somewhere between those for configurations C2 and C4. Since the bond dissociation energy of CO (11.14 eV) is higher than the energy of the VUV photons emitted by the MDHL, CO ice molecules are excited to various states ($A^1\Pi$, $B^1\Sigma^+$, $C^1\Sigma^+$, and $E^1\Pi$), which will subsequently undergo radiationless transitions to the lowest metastable state, $a^3\Pi$, and possibly other metastable states such as $a'^3\Sigma^+$, $d^3\Delta_i$, and $e^3\Sigma^-$. The most probable pathway for breaking the CO bond is through the recombination of two CO molecules, each in a metastable state, or one molecule in a metastable state and the other in an excited state (Zetner et al. 1998; Martin et al. 2000). However, if we take the conversion efficiencies from CO into CO_2 given by Öberg et al. (2007) and Muñoz Caro et al. (2010) into account, less than 5% of CO will be converted into CO_2 from the reaction between metastable and/or excited CO molecules. In other words, more than 95% of the metastable and/or excited CO molecules will transfer their energy to the top monolayer(s) and subsequently lead to desorption induced by electronic transitions (Avouris & Walkup 1989; Öberg et al. 2007; Fayolle et al. 2011).

Since the photodepletion yield in configuration C1 appears to be higher than in configurations C2 and C4 combined, this suggests that the irradiation mechanism in configuration C1 is a more complicated process than we expected, which is discussed in detail in Section 3.3.3. Figure 10 also shows that the photodepletion yields in configurations C3 and C4 were measured to be the same, although those two lamp configurations are, a priori, very different. This interesting coincidence may result from either or any combination of the following: (1) a low proportion of Ly-α photons in these experiments (8.4% and 0%, respectively), (2) the same average photon energy in both configurations (8.60 eV), and (3) similar photon fluxes within 2%.

3.3.2. CO_2 Production from Irradiated CO Ice at 14 K

In order to enhance the accuracy of the measurement of the production of CO_2, the IR beam path of our mid-FTIR system was built inside the UHV chamber to avoid atmospheric CO_2 (gas) interfering with the produced CO_2 (solid) detected in the IR spectra and thus inducing larger error bars on the calculated column density obtained from the $\sim$2340 cm^{-1} band of CO_2 for ice thicknesses larger than 0.05 ML.

Figure 11(a) gives the column density of the produced CO_2 for the four operating configurations as a function of the photon dose and shows that its production follows a similar trend

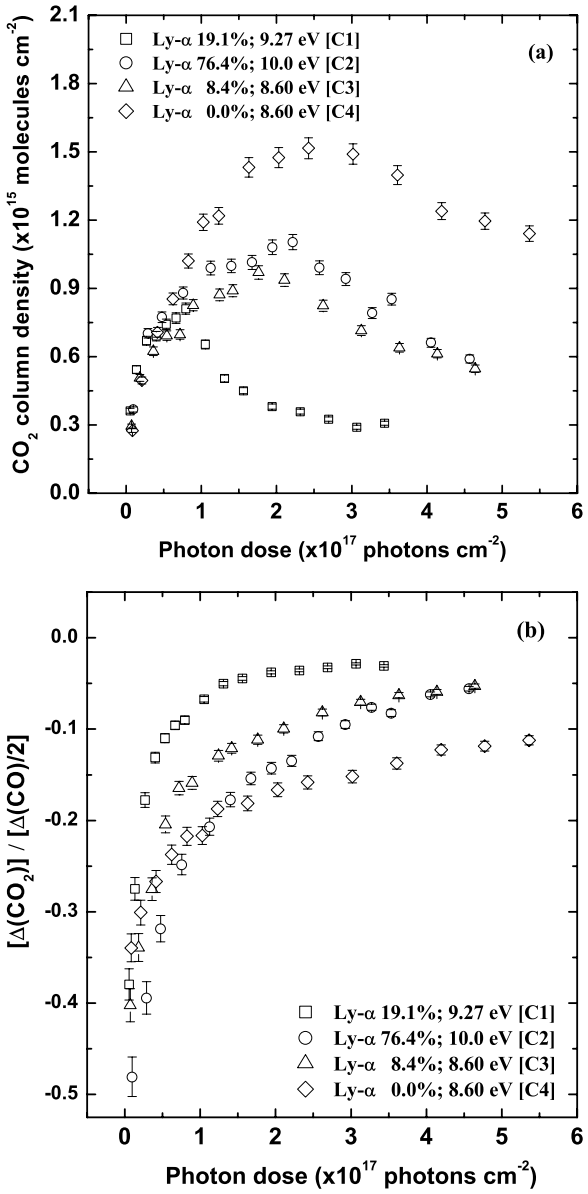

Figure 11. (a) Column density of the CO_2 produced in the CO ice as a function of photon dose when the MDHL is operated in configurations C1–C4 (Table 1). (b) Conversion efficiency of CO into CO_2 as a function of photon dose in the same configurations.

for the four photon energies. The production of CO_2 is not linear, as its rate reaches a maximum, which is different for the four configurations studied here, and then decreases as the produced CO_2 is itself photoprocessed and probably converted into other photoproducts. Figure 11(b) shows the evolution of the parameter $[\Delta(CO_2)]/[\Delta(CO)/2]$ as a function of the increasing photon dose, in which $\Delta(CO_2)$ and $\Delta(CO)$ are the variations of the column densities for CO_2 and CO molecules, respectively. This parameter was chosen because in the present study we assume that CO_2 is mostly produced from the irradiation of CO ice via the reactions

$$CO + h\nu \rightarrow CO^*,$$

$$CO^* + CO \rightarrow CO_2 + C \quad (2)$$

(Luiti et al. 1966; Okabe 1978; Gerakines et al. 1996; Loeffler et al. 2005; Muñoz Caro et al. 2010 and references therein),

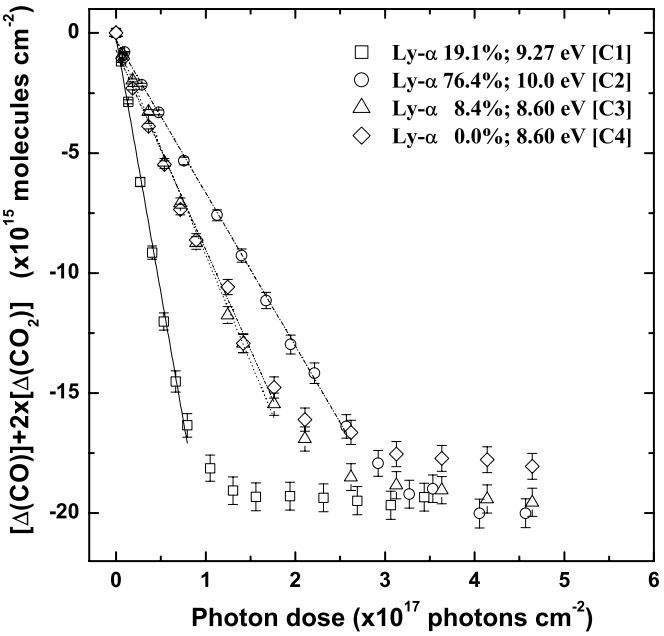

Figure 12. Photodesorbed column density of CO ice irradiated by the MDHL in operating conditions C1–C4 as a function of photon dose, derived after taking the column densities of photodepleted CO and photoproduced CO_2 into account.

where CO^* designates a CO molecule in an excited electronic state. The conversion rate of CO into CO_2, following this reaction mechanism, is not constant over the irradiation period, as it reaches 38%–48% at the beginning of the irradiation (for a photon dose below 2×10^{16} photons cm^{-2}) and then decreases to 3%–12% in the equilibrium domain (photon dose above 3×10^{17} cm^{-2}).

With the exception of configuration C4, in which the MDHL was equipped with a CaF_2 window, the conversion rates into CO_2 in the equilibrium domains are consistent with previously published results (Öberg et al. 2007; Muñoz Caro et al. 2010). The decrease observed after the maximum in the column density of CO_2 in configuration C4 implies that molecular hydrogen emission photons have a lower destruction efficiency for CO_2 than do Ly-α (121.6 nm) photons. This is likely related to the absorption cross section of CO_2 ice in the VUV region (Mason et al. 2006; Cruz-Diaz et al. 2013), which is lower in the molecular hydrogen emission region than at 121.6 nm, so that the number of photons absorbed in that energy range, and consequently the photodestruction rate of CO_2, decreases. In configuration C1, the column density of the produced CO_2 decreases rapidly when the photon dose reaches $\sim 9 \times 10^{16}$ photons cm^{-2}. For the same dose, the photodesorption of CO also decreases abruptly, because the ice thickness becomes smaller than 4 ML (see Figure 1).

3.3.3. Photodesorption Yield of CO at 14 K

The photodesorption of CO ice was monitored by means of both IR and mass spectrometry. The photodesorption yield of CO ice was estimated from our IR data under the assumption that the CO_2 produced during irradiation was correlated with the decrease in column density of CO. This assumption can be justified one considers that the thickness of CO ice was only 22 ML and, therefore, other photoproducts more complex than CO_2 have a very low likelihood of being formed and detected.

Figure 12 shows the evolution of the parameter $[\Delta(CO)] + 2 \times [\Delta(CO_2)]$, derived after taking the column densities of both

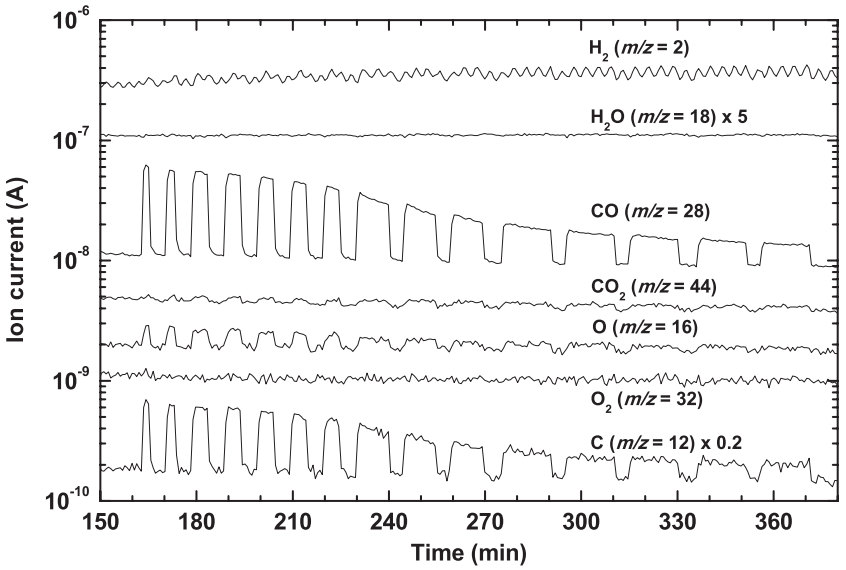

Figure 13. QMS ion currents for several species measured during the VUV irradiation of CO ice at 14 K in configuration C1 (19.1% Ly-α, 9.27 eV average photon energy). The traces shown correspond to the mass of photodesorbed CO ($m/z = 28$ amu) and CO_2 (44 amu), as well as some of their fragments. During VUV irradiation, the ion current for H_2O (18 amu) remains constant at a low level, which indicates that our chamber was practically free from H_2O contamination.

the photodepleted CO and photoproduced CO_2 into account. It shows that the photodesorption of CO ice is a linear function of the photon dose. The production of CO_2 is not linear with respect to the photon dose, but the decrease of the CO ice band is mainly driven by the photodesorption of CO molecules, which is linear with respect to the photon dose until the remaining CO ice is less than 4 ML (see Figure 10). As a result, a linear decrease of the column density of CO during irradiation is observed. An important result of this study is that the conversion rate of CO into CO_2 is high, 38%–48% at the beginning of the irradiation, which has significant astrophysical implications. Since this conversion rate depends on the photon energy distribution, it is important to control the light emitted by an MDHL so that it remains stable during each irradiation interval. Otherwise, a miscalculation of the first data points for the column density of depleted CO ice will result, obscuring the linear correlation shown in Figure 12. The estimated photodesorption yields of CO ice, relative to the total depletion of CO ice during irradiation, are 93%, 91%, 91%, and 85% for configurations C1–C4, respectively.

Mass spectrometry was used to monitor the intensity of the ion currents corresponding to the desorbed molecules. Since the ionization efficiency of the QMS ionizer decreases over time, it must be calibrated before each experiment. This was done during the deposition of CO ice, so that the data reported in the present study take this variation of the QMS ionization efficiency into account. Figure 13 shows the intensities for the ion currents with $m/z = 12$ (assigned to the C generated in the filament of the mass spectrometer from the dissociation of CO, CO_2, and possibly other C-bearing molecules), 18 (H_2O), 28 (CO), 32 (O_2), and 44 (CO_2) amu during the irradiation interval for the experiment in configuration C1. It can be observed that the ion currents for C, CO, and CO_2 suddenly increase when the lamp is turned on and rapidly decrease after it is turned off, in agreement with the data reported in Muñoz Caro et al. (2010). In contrast, the intensities for H_2O and O_2 remain constant during the irradiation, which is consistent with a negligible H_2O and O_2 contamination in our study.

The integration of the ion current for CO ($m/z = 28$ amu) during the full irradiation experiment for the four configurations

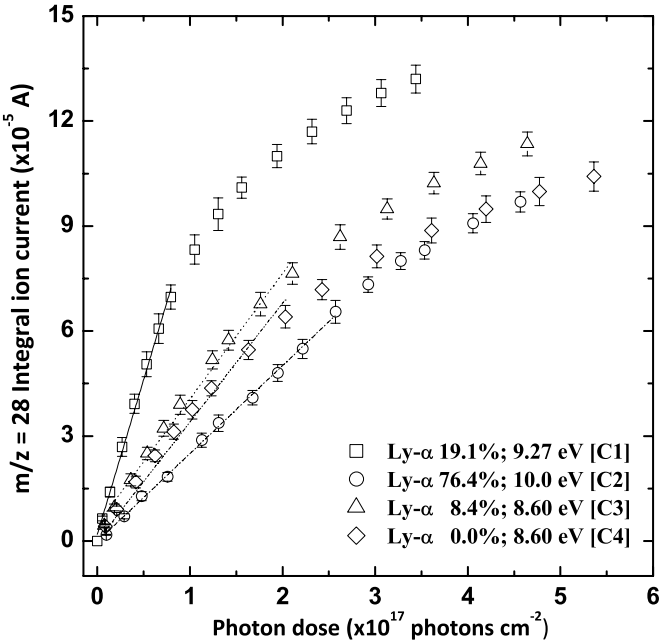

Figure 14. Increase of the accumulated ion current for $m/z = 28$ amu as a function of photon dose for operating configurations C1–C4 (Table 1). The slopes of the linear fits correspond to the partial photodesorption yields of CO ice, which can be compared with the photodesorption yields derived from IR data.

is shown in Figure 14. The ion current for CO is a linear function of the photon dose until the thickness of the ice becomes smaller than 4 ML (this value was estimated by IR spectroscopy; see Figure 10). The integrated ion current for CO is higher for configuration C4 than for configuration C2 in the linear portion of the curve, but they tend to be comparable for higher photon doses. This result is consistent with the IR data, from which we derived that the further destruction of CO_2 was limited in configuration C4 as compared with the others, resulting in a conversion rate of CO into CO_2 about two times higher.

In Section 3.3.1, we found that the photodepletion yield of CO ice in configuration C1 is higher than expected, and the same

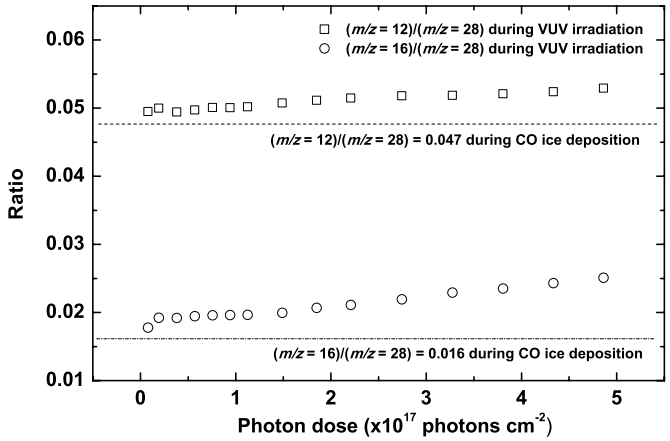

Figure 15. Ratios of the QMS ion currents for $(m/z = 12)/(m/z = 28)$ and $(m/z = 16)/(m/z = 28)$ during CO ice deposition and VUV irradiation at 14 K for the C1 experiment (19.1% Ly-α, 9.27 eV average photon energy).

is observed from both IR and QMS data (Figures 12 and 14). Figure 15 shows that the ratios between, on the one hand, the ion currents for $m/z = 12$ and 28 amu and, on the other, the currents for $m/z = 16$ and 28 amu during the deposition of CO ice are 0.047 and 0.016, respectively. The CO_2 fragmentation in the QMS was also measured during a different pure CO_2 ice deposition experiment (not shown), and the signal ratios of C, O, and CO to CO_2 were 8.9%, 15.9%, and 9.8%, respectively. We used these fragmentation values to calculate the ion intensity of C, O, and CO for which desorbed CO_2 molecules contributed during the VUV irradiation period; these values are 0.2%–1.7%, 1.1%–9.3%, and 0.1%–0.9%, respectively. This means that O and C formation when the lamp is turned on (see Figure 15 in configuration C1) was not mainly caused by photodesorbed CO_2 molecules.

The fact that the 12 amu/28 amu ratio becomes higher than 0.047 during the irradiation period in configuration C1 means that there must be other sources of C atoms, for example, release from the formation of CO_2 (Equation (2)). On the other hand, the fact that the 16 amu/28 amu ratio during the irradiation period in configuration C1 also becomes higher than 0.016 means that there should be extra O atoms released from the destruction by continuous VUV irradiation of the produced CO_2 following

$$CO_2 + h\nu \rightarrow CO + O. \quad (3)$$

The absorption cross section of CO ice in the VUV range is higher in the molecular hydrogen emission region than at 121.6 nm, but the opposite is true for CO_2 ice (Mason et al. 2006; Cruz-Diaz et al. 2013). Therefore, photoprocesses in configuration C1 are more complex than in other experiments, as CO_2 molecules were both produced by hydrogen molecular band irradiation of CO and destroyed by simultaneous Ly-α irradiation. The two photoprocesses described above make the photodesorption yield of CO ice in configuration C1 about two to three times higher than in other configurations.

The photodesorption yields of CO in configurations C1–C4 are listed in Table 2, which shows their values derived from both IR spectroscopy and QMS data. The relative proportions between the photodesorption yields (normalized ratios) obtained from the IR data for the different configurations are strikingly consistent with those obtained from the QMS data. This indicates that the photodesorption yields derived from IR data are in agreement with the photodepletion of CO, which results mainly from the photodesorption and, to a lesser extent, from the production of CO_2. These results show that mass spectrometry is a powerful tool to monitor desorbed species and provide a complementary way to study photodesorption together with IR spectroscopy.

4. CONCLUSIONS AND ASTROPHYSICAL APPLICATIONS

The interstellar radiation field (ISRF) in the VUV region starting at 91.2 nm is a continuum of emission that is well simulated by MDHL spectra (Mathis et al. 1983; Jenniskens et al. 1993; Muñoz Caro & Schutte 2003), with the exception of emission in the 91.2–114 nm range, which cannot be reproduced in our laboratory experiments because of the MgF_2 window's cutoff. The extinction inside a dense cloud will attenuate the most energetic photons, which affects the Ly-α component, more effectively than less energetic photons, including the molecular hydrogen emission bands (Goicoechea & Le Bourlot 2007). At an extinction of about $A_V = 3$, there is no penetration of the external VUV field in the cloud for the mean intensity of the ISRF (Mathis et al. 1983).

Secondary VUV photons generated by interaction between cosmic rays and molecular hydrogen in dense interstellar clouds display a large number of narrow lines in the 91.2–170 nm range, with broader emission bands at molecular hydrogen wavelengths (Gredel et al. 1987). The MDHL can also be used to mimic the secondary VUV photons inside dense clouds, except for photons that are more energetic than hydrogen Ly-α ($\lambda <$ 121.6 nm), as a result of the aforementioned MgF_2 cutoff.

VUV spectroscopic measurements of the MDHL show that its photon energy distribution is a function of (1) the pressure of hydrogen flowing in the lamp, with the position of the pressure gauge also being important, (2) the composition and optical quality of the window (MgF_2 versus CaF_2), (3) the lamp geometry (F-type versus T-type geometries), and (4) the nature of the discharged gas (pure H_2 versus H_2 mixed with He or Ar). Different combinations of these parameters lead to different energy distributions of the photons irradiating the samples and consequently to significant differences in the resulting photoinduced processes. The great majority of previous studies dedicated to VUV irradiation of astrophysical ice analogs have not taken into consideration the emission spectrum of the MDHL. Our work provides this information for future studies. The photodepletion yield of CO ice is much higher in configuration C1 than in C2–C4, while the total flux and average photon energies are within the same range. This indicates that the different energy distribution in configuration C1 is the main parameter responsible for the high photodepletion measured in this experiment.

IR spectroscopy data show that the photodesorption yield of CO ice mostly induced by Ly-α photons (121.6 nm) is smaller than that induced by the photons emitted from the molecular hydrogen bands (140–170 nm). However, the photodesorption yield induced by a combination of Ly-α and molecular hydrogen emission is two to three times higher than in the cases where only one region of the VUV spectrum is used. This indicates that the photodesorption of CO ice induced by a nonmonochromatic light source, such as that emitted by an MDHL, is a photochemical process that is more complex than expected from the absorption spectrum of CO ice in the 114–180 nm range. This finding has important astrophysical implications, as it means that understanding the effects of the ISRF and secondary photon irradiations on ice mantles requires, in addition to monochromatic VUV sources, the use of continuum emission sources such as

the MDHL in various configurations (providing various spectral properties).

CO molecules that are not photodesorbed are mostly converted into CO_2, with a conversion rate that reaches 38%–48% at the beginning of the irradiation (when the photon dose is lower than 2×10^{16} photons cm^{-2}) and drops to 3%–5% (12% when a CaF_2 window is used, configuration C4, no Ly-α emission) when the system reaches an equilibrium. The CO-to-CO_2 conversion rate in configuration C4 (no Ly-α emission) was found to be about three to four times higher than those for the three other lamp configurations, as a result of the fact that CO_2 is itself more easily photodestroyed when subjected to continuous VUV irradiation with photon energies higher than 10.1 eV ($\lambda < 123.0$ nm).

The photodepletion of CO can therefore be explained by two independent processes, namely, photolysis and photoinduced desorption. Photolysis leads to the destruction of the parent molecules to convert them into other products by means of radical–radical and radical–molecule reactions, whereas photodesorption does not involve any dissociation of parent molecules but provides them enough energy to be sputtered out of the ice surface and become free gas-phase particles. Consequently, the depletion of CO molecules in our experiments can probably only be due to either their conversion into other products or their photodesorption.

Infrared observations of icy grain mantles in dark interstellar clouds and circumstellar environments show evidence for CO mixed with CO_2 in the ices (Pontoppidan et al. 2008; Kim et al. 2012). The high conversion rate of CO into CO_2 for low photon doses reported here provides an efficient mechanism for the formation of CO_2 in the bulk of ice mantles containing CO if the ice is exposed to VUV photons. For higher doses, photodesorption of CO is found to be the dominant process.

This work was supported by Taiwan National Science Council grant NSC99-2112-M-008-011-MY3 (T.-S.Y.), National Central University under a grant from the Aim for Top University Project (W.-H.I.), the Spanish MICINN/MINECO under projects AYA2011-29375 and CSD2009-00038 (G.M.M.C.), and the NSF Planetary Astronomy Program under grant AST-1108898 (C.-Y.R.W.).

REFERENCES

Alves, J., Lada, C. J., & Lada, E. A. 1999, ApJ, 515, 265
Avouris, P., & Walkup, R. E. 1989, ARPC, 40, 173
Bennett, C. J., & Kaiser, R. I. 2007, ApJ, 660, 1289
Bergin, E. A., Ciardi, D. R., Lada, C. J., et al. 2001, ApJ, 557, 209
Cecchi-Pestellini, C., & Aiello, S. 1992, MNRAS, 258, 125
Chen, Y. J., Nuevo, M., Hsieh, J.-M., et al. 2007, A&A, 464, 253
Cottin, H., Moore, M. H., & Benilan, Y. 2003, ApJ, 590, 874
Cruz-Diaz, G. A., Muñoz Caro, G. M., Chen, Y.-J., & Yih, T.-S. 2013, A&A, accepted
d'Hendecourt, L. B., Allamandola, L. J., Baas, F., & Greenberg, J. M. 1982, A&A, 109, L12
d'Hendecourt, L. B., Allamandola, L. J., & Greenberg, J. M. 1985, A&A, 152, 130
Duley, W. W., & Williams, D. A. 1993, MNRAS, 260, 37
Fayolle, E. C., Bertin, M., Romanzin, C., et al. 2011, ApJL, 739, L36
Gerakines, P. A., Moore, M. H., & Hudson, R. L. 2000, A&A, 357, 793
Gerakines, P. A., Schutte, W. A., & Ehrenfreund, P. 1996, A&A, 312, 289
Goicoechea, J. R., & Le Bourlot, J. 2007, A&A, 467, 1
Gredel, R., Lepp, S., & Dalgarno, A. 1987, ApJL, 323, L137
Greenberg, J. M., & Yencha, A. J. 1973, in IAU Symp. 52, Interstellar Dust and Related Topics, ed. J. M. Greenberg & H. C. van de Hulst (Dordrecht: Reidel), 369
Jenniskens, P., Baratta, G. A., Kouchi, A., et al. 1993, A&A, 273, 583
Jiang, G. J., Person, W. B., & Brown, K. G. 1975, JChPh, 64, 1201
Kim, H. J., Evans, N. J., II, Dunham, M. M., Lee, J.-E., & Pontoppidan, K. M. 2012, ApJ, 758, 38
Knapp, R. A., & Smith, A. M. 1964, ApOpt, 3, 637
Lee, C.-W., Kim, J.-K., Moon, E.-S., et al. 2009, ApJ, 697, 428
Léger, A., Jura, M., & Omont, A. 1985, A&A, 144, 147
Leto, G., & Baratta, G. A. 2003, A&A, 397, 7
Loeffler, M. J., Baratta, G. A., Palumbo, M. E., et al. 2005, A&A, 435, 587
Lu, H.-C., Chen, H.-K., Cheng, B.-M., et al. 2005, JPhB, 38, 3693
Luiti, G., Dondes, S., & Harteck, P. 1966, JChPh, 44, 4051
Martin, J.-P, Perrin, M.-Y., & Porshnev, P. I. 2000, CPL, 332, 283
Mason, N. J., Dawes, A., Holton, P. D., et al. 2006, FaDi, 133, 311
Mathis, J. S., Mezger, P. G., & Panagia, N. 1983, A&A, 128, 212
Moore, M. H., & Hudson, R. L. 1998, Icar, 135, 518
Muñoz Caro, G. M., Jiménez-Escobar, A., Martin-Gago, J. A., et al. 2010, A&A, 522, A108
Muñoz Caro, G. M., & Schutte, W. A. 2003, A&A, 412, 121
Nygaard, K. J. 1964, BJAP, 15, 597
Öberg, K. I., Fuchs, G. W., Awad, Z., et al. 2007, ApJL, 662, L23
Öberg, K. I., van Dishoeck, E. F., & Linnartz, H. 2009, A&A, 496, 281
Okabe, H. 1978, Photochemistry of Small Molecules (New York: Wiley)
Palumbo, M. E., Baratta, G. A., & Spinella, F. 2006, MSAIS, 9, 192
Pontoppidan, K. M., Boogert, A. C. A., Fraser, H. J., et al. 2008, ApJ, 678, 1005
Prasad, S. S., & Tarafdar, S. P. 1983, ApJ, 267, 603
Samson, J. A. R. 1967, Techniques of Vacuum Ultraviolet Spectroscopy (New York: Wiley)
Schutte, W. A., & Greenberg, J. M. 1991, A&A, 244, 190
Shen, C. J., Greenberg, J. M., Schutte, W. A., & van Dishoeck, E. F. 2004, A&A, 415, 203
Tielens, A. G. G. M., & Hagen, W. 1982, A&A, 114, 245
Warnek, P. 1962, ApOpt, 1, 721
Watanabe, N., Horri, T., & Kouchi, A. 2000, ApJ, 541, 772
Watanabe, N., Mouri, O., Nagaoka, A., et al. 2007, ApJ, 668, 1001
Weber, P., & Greenberg, J. M. 1985, Natur, 316, 403
Westley, M. S., Baragiola, R. A., Johnson, R. E., & Baratta, G. A. 1995, P&SS, 43, 1311
Willacy, K., & Millar, T. J. 1998, MNRAS, 298, 562
Wu, C. Y. R., Judge, D. L., Cheng, B.-M., et al. 2002, Icar, 156, 456
Wu, C. Y. R., Judge, D. L., Cheng, B.-M., et al. 2003, JGR, 108, 5032
Wu, Y.-J., Wu, C. Y. R., Chou, S.-L., et al. 2012, ApJ, 746, 175
Zetner, P. W., Kanik, I., & Trajmar, S. 1998, JPhB, 31, 2395